ADVANCED MATERIALS
www.advmat.de

Sensing of COVID-19 Antibodies in Seconds via Aerosol Jet Nanoprinted Reduced-Graphene-Oxide-Coated 3D Electrodes

*Md. Azahar Ali, Chunshan Hu, Sanjida Jahan, Bin Yuan, Mohammad Sadeq Saleh, Enguo Ju, Shou-Jiang Gao, and Rahul Panat**

Rapid diagnosis is critical for the treatment and prevention of diseases. An advanced nanomaterial-based biosensing platform that detects COVID-19 antibodies within seconds is reported. The biosensing platform is created by 3D nanoprinting of three-dimensional electrodes, coating the electrodes by nanoflakes of reduced-graphene-oxide (rGO), and immobilizing specific viral antigens on the rGO nanoflakes. The electrode is then integrated with a microfluidic device and used in a standard electrochemical cell. When antibodies are introduced on the electrode surface, they selectively bind with the antigens, changing the impedance of the electrical circuit which is detected via impedance spectroscopy. Antibodies to SARS-CoV-2 spike S1 protein and its receptor-binding-domain (RBD) are detected at a limit-of-detection of 2.8×10^{-15} and 16.9×10^{-15} M, respectively, and read by a smartphone-based user interface. The sensor can be regenerated within a minute by introducing a low-pH chemistry that elutes the antibodies from the antigens, allowing successive sensing of test samples using the same sensor. Sensing of S1 and RBD antibodies is specific, which cross-reacts neither with other antibodies such as RBD, S1, and nucleocapsid antibody nor with proteins such as interleukin-6. The proposed sensing platform could also be useful to detect biomarkers for other infectious agents such as Ebola, HIV, and Zika.

Pandemics and epidemics caused by emerging infectious agents such as SARS-CoV, SARS-CoV-2, influenza virus, ZIKA virus, and Ebola virus have seriously affected human health, and led to lost economic activity and challenged health-care systems.[1] Recently, SARS-CoV-2 has caused the COVID-19 pandemic with a significant global impact.[2] Several approaches involving advanced materials are being explored for therapeutics for the treatment of COVID-19.[3] While these efforts address the treatment side, advanced materials can also be used to create new paradigms in testing for the disease that can play a pivotal role in the combat against epidemics. A rapid detection of the infection would allow isolation of patients and contact tracing that can save lives and help resume economic activity. Even after opening of the economy, secondary spikes are likely to occur, requiring low-cost, rapid methods for early detection of the infection. This is especially true since a significant proportion of the patients transmitting the disease are asymptomatic.[4] In addition, a generic device, if developed, can be of immense use for the detection of biomarkers for a variety of diseases, benefiting public health.

Two primary approaches have been used to detect the COVID-19 infection. The first approach utilizes the genetic sequence of the virus and includes genomic sequencing, CRISPR-based test (CRISPR = clustered regularly interspaced short palindromic repeats),[5] and reverse transcription real time quantitative polymerase chain reaction (RT-qPCR).[5,6] These methods are relatively accurate but are generally slow because of multiple sample processing steps and the need to ship the sample to a testing laboratory. The accuracy of these methods is also dependent upon the protocol of sampling, preservation, transportation, and processing of the samples.[7] Since the viral RNA polymerase does not possess the proof-reading function, it leads to a high mutation rate. As a result, the accuracy of these methods is compromised if the virus mutates in the targeting genomic region, which occurs frequently.[8] The second approach is to detect specific antibodies to the viral antigens.[9] These serological methods include enzyme-linked immunosorbent assay (ELISA) and lateral flow immunoassay, some of which often give on-site results within ten minutes without requiring sophisticated sample preparation.[10] Current assays for detection of COVID-19 infections are based on structural proteins including spike proteins (S-proteins) and/or nucleocapsid protein (N-protein).[11] These assays have a relatively low sensitivity, a false positive rate of

Dr. Md. A. Ali, C. Hu, S. Jahan, Dr. B. Yuan, Dr. M. S. Saleh, Prof. R. Panat
Department of Mechanical Engineering
Carnegie Mellon University
Pittsburgh, PA 15213, USA
E-mail: rpanat@andrew.cmu.edu
Dr. E. Ju, Prof. S.-J. Gao
Cancer Virology Program
UPMC Hillman Cancer Center and Department of Microbiology and Molecular Genetics
University of Pittsburgh School of Medicine
Pittsburgh, PA 15213, USA
The ORCID identification number(s) for the author(s) of this article can be found under https://doi.org/10.1002/adma.202006647.

DOI: 10.1002/adma.202006647

about 5–11%,[9] and usually a long sample preparation time of at least 0.5–2 h. Note that the antibody testing platforms can reveal the dynamics of immune response for COVID-19 infection.[12] The types and titers of antibodies vary at different stages of viral infection for both symptomatic and asymptomatic patients.[13] Most of the individuals who have recovered from the SARS-CoV-2 infection have antibodies due to immune response.[14] It has also been found that the existence of a very low concentration of antibodies in blood samples due to lack of sufficient cellular immunity may hinder recovery. A recent study showed a detection sensitivity of 11.1% at the early stage (1–7 days), 92.9% at intermediate stage (8–14 days) and 96.8% at late stage (more than 15 days) for the immunoglobin G (IgG) antibody test of 134 samples from 105 COVID-19 patients.[13] For late-stage viral infection, the antibody test shows a 100% sensitivity.[15] The exact molar concentrations of the antibodies in blood at these stages are still not well documented and are likely to vary widely across patients. In addition, antibody testing can verify if the vaccines are working during clinical trials, and establish the fraction of asymptomatic cases in a given population.[16] Also, this rapid test could be a complementary modality to nucleic acid tests, which can provide the immunological evidence for physicians to make accurate diagnostic and pretreatment decisions.

There is thus an urgent need to develop a sensitive and specific assay for rapid detection of antibodies to SARS-CoV-2 infection within minutes, or if possible, seconds; ideally within days of infection, which could particularly be useful for medically underserved areas if the readout is enabled by a smartphone. Electrochemical sensing is a promising method for the detection of pathogens or antibodies.[17] In this method, the formation of antibody–antigen complex is detected via electrochemical transduction. The sensitivity, specificity, and speed of detection, however, will depend upon the electrochemical cell and the geometry and surface chemistry of the electrodes, in addition to the antigen and assay procedures. In conventional electrochemical sensors, the electrodes are typically planar 2D structures which are often decorated with nanomaterials to increase their surface area.[18]

We note that the sophistication of biosensing devices has evolved with the developments in microelectronics—moving from bio-MEMS to miniaturized lab-on-chip constructs made by advanced photolithographic techniques.[19] Recently, nanoparticle-based 3D-printing methods involving advanced materials have emerged in microelectronics that enable intricate geometries, material combinations, and custom microstructures. These methods offer many exciting advantages over conventional lithography such as a simple two-step fabrication process controlled by computer-aided design (CAD) programs, customizability, and prototypability. Amongst the different additive manufacturing methods, Aerosol Jet (AJ) 3D printing is a technique that uses a stream of aerosolized droplets to deposit an array of nanomaterials at a resolution of 10 µm and has been used to fabricate various electronic devices.[20] Until recently, AJ printing was primarily used to create 2D planar structures as electronic components in devices.[21] Recently, however, Saleh et al.[22] have used the dynamics of the aerosol microdroplets to create 3D device geometries with aspect ratios as high as 50:1, providing pathways to create complex and intricate geometries with high surface-to-volume ratios for electrodes.

The work presented in this paper was thus motivated by two factors. First, we aimed to utilize the latest advances in materials and manufacturing methods such as nanoparticle 3D printing to create a device that rapidly detects COVID-19 antibodies. The focus was to use AJ nanoparticle 3D printing to create 3D electrode geometry and develop a unique reduced graphene oxide (rGO)-based surface chemistry with viral antigens that significantly enhances the transport of diffusing species in an electrochemical cell. The second aim was to use electrochemical transduction to detect COVID-19 antibodies within seconds and with a regeneration capability, along with a readout enabled by a smartphone-based platform. The focus was to develop a chemistry that can regenerate the device within a minute and establish selectivity, sensitivity, reproducibility, and repeatability of this sensor platform.

We first describe a 3D-printed COVID-19 test chip (3DcC) platform. The schematic of the 3DcC device along with AJ nanoprinting of the 3D electrodes is shown in **Figure 1**. The functionalization of 3D electrodes by rGO nanoflakes and viral antigens is also a critical step in the formation of the 3DcC device and is described in **Figure 2**. Although details of the fabrication process are given in the Experimental Section, the device construction and surface chemistry are central to the function of the sensor and hence briefly described below. Figure 1a shows a glass slide coated with patterned chromium (5 nm thick) and gold (100 nm thick) which formed the base layer of the three electrodes (working electrode or WE, counter electrode or CE, and reference electrode or RE) of an electrochemical cell. Figure 1b shows the AJ printing process of the micropillar array on the WE shown in Figure 1a. The AJ printer breaks the gold nanoparticle ink in the vial via ultrasonication into microdroplets, each containing the gold nanoparticles (2–5 nm in diameter). The microdroplets were carried to the nozzle via an inert gas (N_2) and aerodynamically focused on the WE, which was heated to 150 °C. Figure 1c,d shows a CAD controlled process of droplet dispense to form individual pillars. The deposition was in the form of micro-rings of gold nanoparticle ink. Once one layer was printed, the solvent evaporated due to the heat from the substrate, forming solidified "dry" material containing the nanoparticles and binders. When the next ring was printed, the surface tension of the solvent in the ring allowed the micropillars to be built without the use of any support structures. Each layer of the rings was about 5–10 µm thick and formed within a fraction of a second. A succession of these processes formed a 10×10 micropillar array consisting of unsintered nanoparticles and binders. Upon sintering of the printed structure, the gold micropillars for the electrode were formed. Figure 1e shows the schematic of the construction of the PDMS housing by a replica-molding method, which involved using a poly(methyl methacrylate) (PMMA) mold and a poly(dimethylsiloxane) (PDMS) reverse-mold to create a PDMS microfluidic channel. The RE, shown in Figure 1a was coated with a thin silver/silver chloride (Ag/AgCl) layer by using a shadow mask. The PDMS housing was then placed manually on the glass slide containing the micropillar array electrode and other electrodes (CE and RE). The complete construction of the 3DcC device is shown in Figure 1f. Note that fluid could be introduced in the device by tubes inserted into the microfluidic channel.

An important step in the working of the 3DcC device is the functionalization of the 3D-printed microelectrode by viral

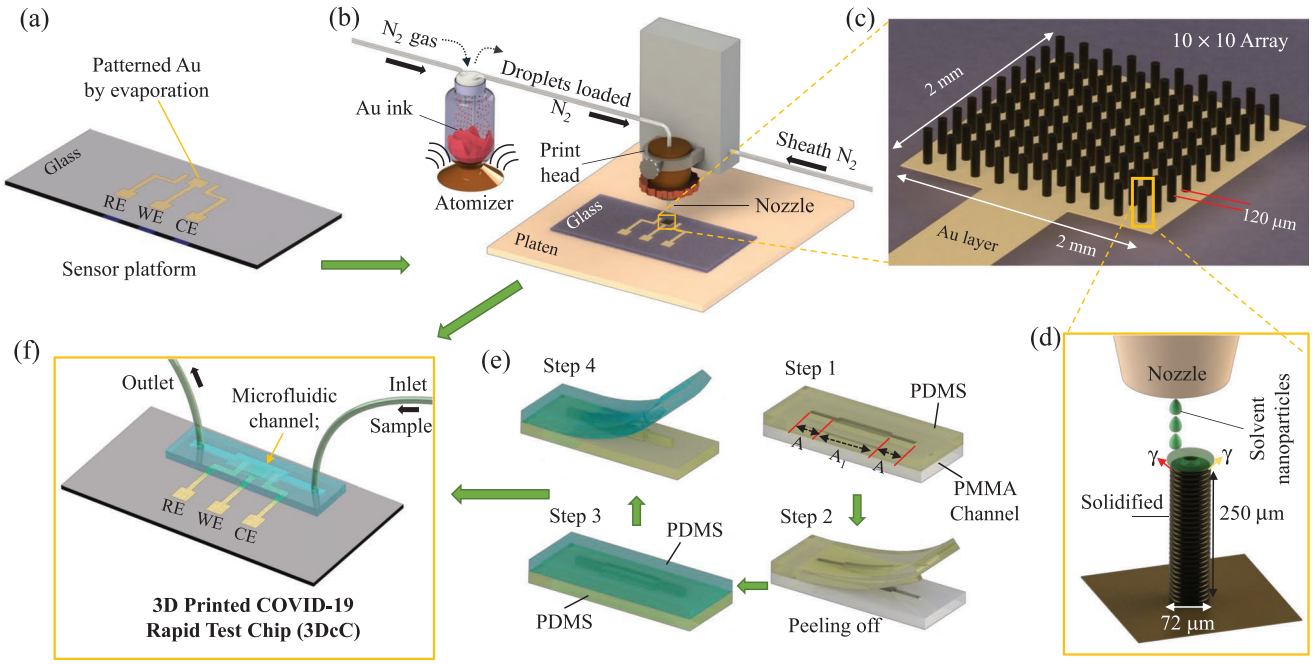

Figure 1. Schematic of the manufacturing process of the 3D-printed COVID-19 test chip (3DcC) by Aerosol Jet nanoparticle 3D printing. a) Glass substrate with patterned gold film forming the base for working electrode (WE), counter electrode (CE), and reference electrode (RE) of the electrochemical cell of 3DcC. b) Construction of Aerosol Jet machine where gold ink is converted into an aerosol consisting of micro-droplets using ultrasonic energy and transported to a nozzle by nitrogen (N_2) gas where it is focused on the gold film of the WE using a sheath gas (also N_2) to form the micropillars. The entire process is digitized with the CAD program controlling the printing process. c) An AJ-printed 10 × 10 gold micropillar array where pillar-to-pillar gap is indicated. d) Details of AJ printing of a single micropillar where rapid layer-by-layer stacking of the micro-rings of the nanoparticle ink are achieved using surface tension (γ) of the printed ink. The entire process is achieved without the use of any support structure. Once a layer was printed, the ink loses solvents due to the heat from the platen (which was heated to 150 °C using a custom heater). The dried ink provides a base to receive the next micro-ring; and the process is repeated. e) Process of fabrication of the PDMS housing of the 3DcC device. A PDMS structure is created using a PMMA master mold using replica molding. The dimensions of sections A and A1 are $1 \times 1 \times 5$ mm^3 and $2 \times 1 \times 10$ mm^3, respectively. This structure then acts as a reverse-mold for the PDMS housing that contains a cavity for microfluidic channel as shown. f) The 3DcC device formed by placing the PDMS housing with microfluidic channel on the glass substrate with the micropillar electrodes. Prior to this step, the micropillar electrodes were functionalized with reduced graphene oxide (rGO) and viral antigens as described in Figure 2.

antigens using rGO nanoflakes for detection of antibodies from the fluid introduced in the electrochemical cell. This process is depicted in Figure 2a–d. The bare 3D micropillar electrode is shown in Figure 2a. The micropillar electrode array functionalized using rGO nanoflakes is shown in Figure 2b. The carboxylated (−COOH) groups of rGO are also shown in the Figure 2b. Due to the π–π interactions amongst the coated rGO, the coating was expected to be non-uniform.[23] Figure 2c shows antigens bonded with the rGO nanoflakes of the electrode. This was achieved by activating the −COOH groups of rGO using a coupling chemistry of EDC:NHS (1-ethyl-3-(3-dimethylaminopropyl) carbodiimide, *N*-Hydroxy-Succinimide).[24] This chemistry facilitates the formation of C−N co-valent bonding between rGO and antigens via an amidation reaction.[24] Specifically, this reaction involved the EDC molecules acting as cross-linkers between −COOH and $-NH_2$ (i.e., amine group of the viral antigens) and NHS molecules acting as stabilizers during this reaction.[24] Two SARS-CoV-2 antigens, namely, spike S1 and receptor-binding domain (RBD), were separately used in this process (in different sensors). Schematic in Figure 2d shows antibodies selectively binding with the antigens when a fluid containing antibodies was introduced in the chamber. It is noted that a treatment with bovine serum albumin (BSA) molecules was used to block non-specific sites of the sensor. The details of the electrode surface functionalization are described in the Experimental Section.

The 3DcC device works on the principle of electrochemical transduction.[25] When an AC potential is applied between WE and RE, an electrical double layer is formed at the WE-electrolyte interface (Figure 2e). For an electrolyte such as ferro/ferricyanide, the double layer can be formed due to accumulation of oppositely charged ions at the interface compared to the charge on the electrode (Figure 2e). This creates a characteristic impedance when a constant potential is applied between, WE and RE. An equivalent circuit is shown in Figure 2e, where C_{dl} is the double layer capacitance, R_{ct} is the charge transfer resistance, and R_s is the electrolyte resistance. Note that in the current study, the electrolyte used was phosphate buffer saline solution mixed with ferro/ferricyanide. When a fluid containing antibodies to the viral antigens shown in Figure 2c are introduced in the microfluidic chamber, we expect selective binding of the target antibodies to the corresponding antigens on the electrode, which would increase the thickness of C_{dl} layer, causing a higher R_{ct}, which could then be detected via

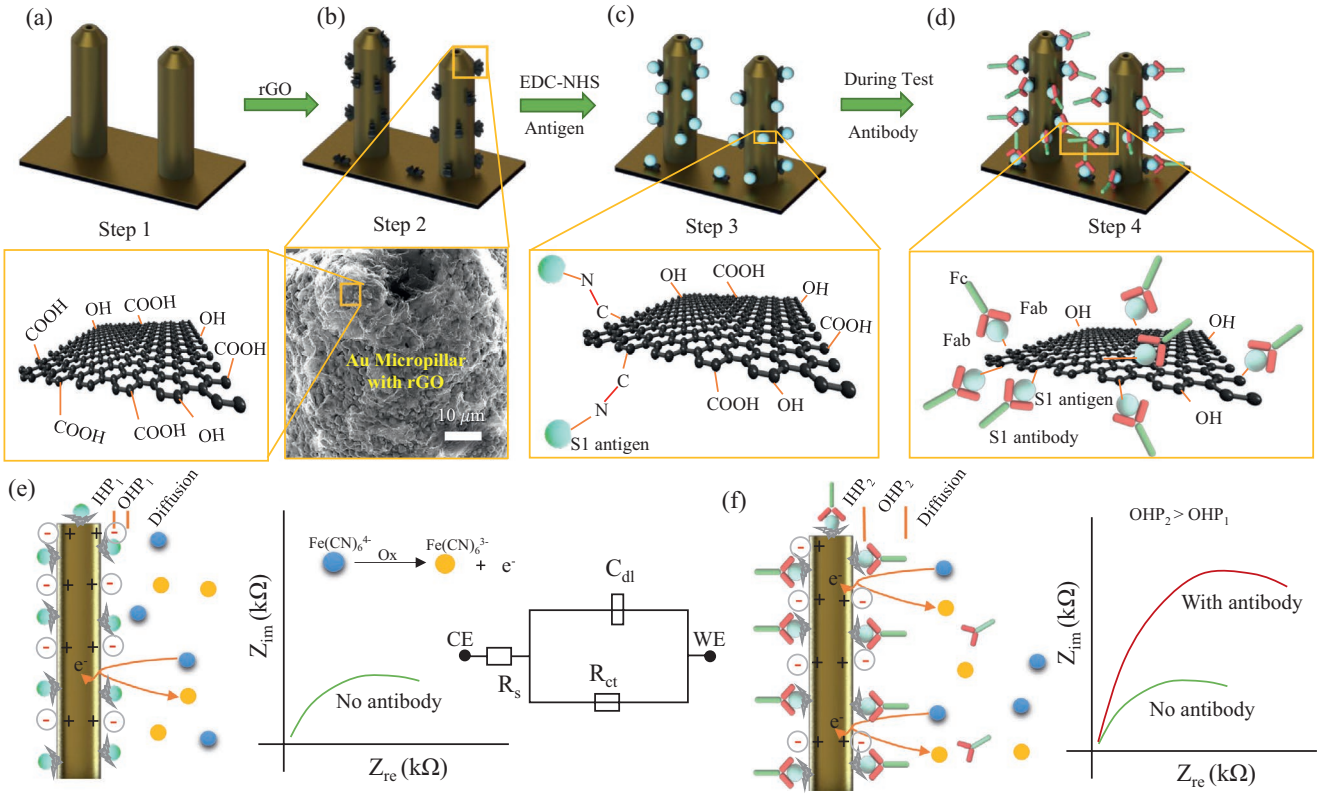

Figure 2. Functionalization of 3D-printed micropillar electrode and 3DcC sensor operation. a) AJ-printed gold micropillars prior to the surface treatment (step 1). b) Coating of the electrodes by carboxylated (—COOH) rGO sheets by a simple drop-casting process (step 2). An SEM image shows the decoration of rGO sheets on the gold pillar. The electrostatic or van der Waals interactions allow the rGO sheets to be connected to the micropillar. The surface porosity of the 3D-printed micropillar shown in the SEM images in Figure 3c likely aid in this process. Molecular structure of a rGO sheet is shown where —COOH and —OH groups are indicated. c) Coupling of the viral antigens with the rGO sheets using EDC:NHS chemistry (step 3). The EDC and NHS molecules activate the —COOH group of rGO sheets. Recombinant antigens of the SARS-CoV-2 are immobilized and bound to rGO sheets by establishing strong covalent bonds between the —COOH group of rGO and $—NH_2$ group of antigens via an amidation reaction. Two antigens, namely, spike S1 and RBD, were separately immobilized in this manner. Bovine serum albumin (BSA) treatment on the pillar surface blocked the non-specific sites of the sensor. d) Antibodies selectively attached to the specific antigens upon introduction to the sensor via an antibody–antigen interaction (step 4). e,f) Schematics showing the sensing principle of the 3DcC device. The electrode/electrolyte interface of the WE was expected to form an electrical double layer (C_{dl}), inner Helmholtz plane or IHP, outer Helmholtz plane or OHP, and a diffusion layer during the redox reaction. An equivalent electrical circuit is shown. When antibodies are introduced (f), they rapidly bind with the antigens on the electrode surface, altering the Nyquist plot (schematics in (e) and (f)) which is captured by electrical impedance spectroscopy (EIS).

electrochemical impedance spectroscopic (EIS) measurements (Figure 2f). First, we expect the 3D geometry to accelerate the formation of the electrical double layer compared to a corresponding 2D surface, enabling a fast detection of the changes in R_{ct} and an increase in the sensitivity. Further, we expect that binding of the antibodies with antigens will increase the thickness of the double layer, causing the R_{ct} to increase proportionally. Thus, simple measurements of R_{ct} values would provide an excellent measure of the presence of antibodies in the fluid introduced in the 3DcC device.

Figure 3 shows the microscopy and spectroscopy analysis of 3DcC device constructed using the processes shown in Figures 1 and 2. An optical micrograph of the device with CE, WE, and RE is shown in Figure 3a. The scanning electron microscopy (SEM) images of 3D gold micropillar array electrode (i.e., WE) fabricated by AJ printing prior to rGO and antigen functionalization is shown in Figure 3b,c. The average and standard deviation of pillar height, pillar diameter, and pillar-to-pillar distance are 249.3 ± 6.7, 73.2 ± 2.3, and 118.3 ± 2.2 µm, respectively when measured at six random locations across five sensors (see Figure S1 in the Supporting Information).

The top surface of solid pillar had a 15 µm deep and 20 µm diameter dip which was a result of the printing process depicted in the schematic of Figure 1d. The surface texture of the gold pillars formed by nanoparticle sintering is shown in the zoomed-in SEM images of Figure 3c and Figure S2a (Supporting Information). This texture consisted of micrometer-sized gold crystals on the pillar surface and a surface porosity caused by the nanoparticle sintering process. This surface texture was expected to provide additional sites for rGO adhesion in addition to increasing the total surface area. The micropillar electrode after the rGO and antigen treatment (Figure 2c) is shown in Figure 3d and Figure S2c (Supporting Information). Figure 3d shows the rGO nanoflakes attached to the gold micropillars as well as the gold base layer (also see Figure S2c in the Supporting Information). Graphene nanoflakes appeared wrinkled on the Au surface (zoomed-in images of Figure S2b,c

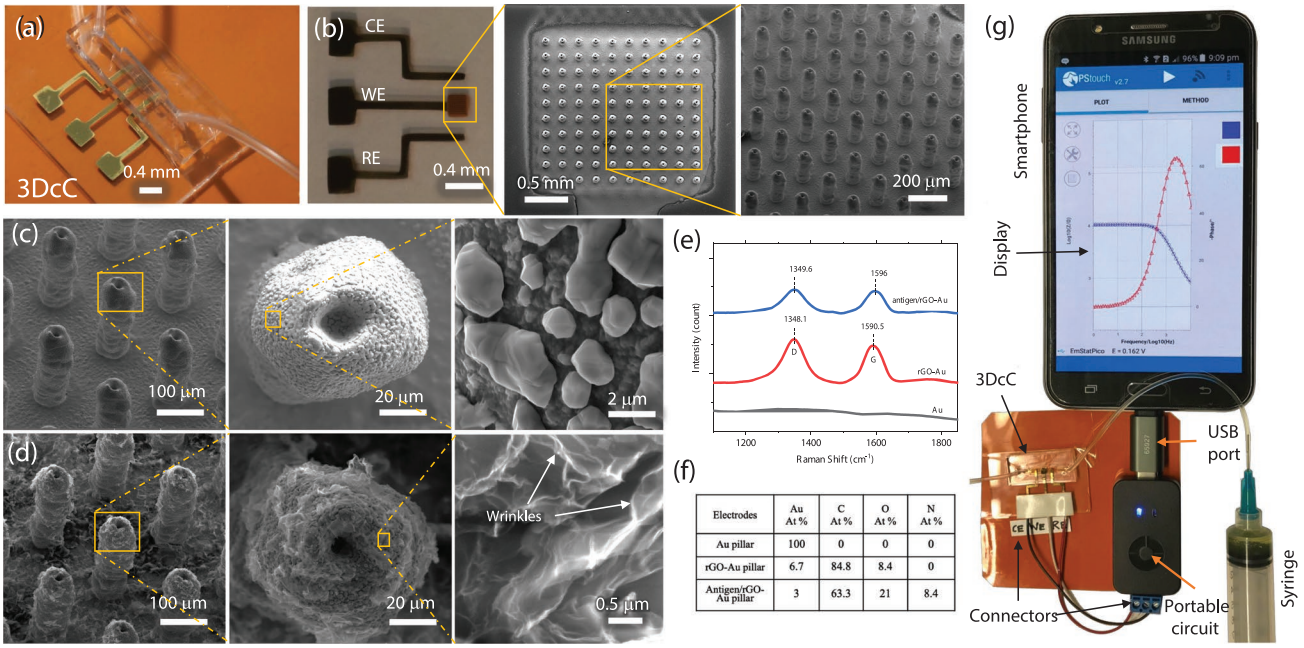

Electrodes	Au At %	C At %	O At %	N At %
Au pillar	100	0	0	0
rGO-Au pillar	6.7	84.8	8.4	0
Antigen/rGO-Au pillar	3	63.3	21	8.4

Figure 3. Physical and chemical characterization of the 3DcC device. a) An optical image of the 3DcC device made by the fabrication process described in Figures 1 and 2. b) Optical and SEM images of the AJ-printed gold micropillar array (10 × 10) at different magnifications. c) SEM images showing the morphology of a single gold micropillar at different magnifications. The tips of the micropillars are pointed and have a small circular dip at the top (diameter 20 µm) which is a result of the printing process described in Figure 1d. Surface morphology of the micropillars consisted of gold clusters that created a characteristic surface porosity. This morphology helps attach rGO flakes to the electrode surface. d) SEM images showing the morphology of a gold micropillar after rGO decoration. The rGO sheets have formed secondary 3D networks adjacent to the micropillars. The rGO has also formed wrinkles likely due to π–π interactions amongst graphene sheets. e) Raman spectra of an AJ-printed gold micropillars without coating, after coating with rGO, and after immobilization of antigens on rGO–Au. The spectra show both defect and graphitic peaks for the coated samples. The graphitic peak is shifted to higher frequency upon S1 antigen immobilization. f) EDX studies showing composition (in atomic %) before coating, after coating with rGO, and after immobilization of antigens on rGO–Au. g) The 3DcC device interfaced with a portable potentiostat which was connected to a smartphone via a USB-C connection to record the signal using PStouch software.

in the Supporting Information) which was expected to enhance the loading capacity of the antigens.

Raman spectroscopic measurements were conducted to investigate the defect (D) and graphitic (D) bands present in the rGO–Au micropillars (Figure 3e) with and without antigens. The Au micropillar surface prior to rGO treatment did not show any Raman peaks. The Raman spectrum of rGO–Au micropillars revealed a D-band at 1348.1 cm^{-1} and a G-band at 1590.5 cm^{-1}. The D-band (symmetry A1g mode) is due to the vibration of –sp^3 carbon atoms or defects while G-band originates due to first-order scattering of E2g phonon of sp^2 carbon atoms at the center of Brillion zone.[26] The D and G peaks in the Raman spectrum indicate the presence of rGO sheets on gold pillars. The intensity ratio (I_D/I_G) of rGO–Au was 0.84, which was slightly changed to 0.85 after incorporation of antigens. Antigen immobilization on rGO sheets influenced the peak position, which was shifted to higher wavenumber (5.5 cm^{-1}) due to the decreased graphitic nature of the rGO sheets. Energy-dispersive X-ray (EDX) studies indicated presence of large amount of carbon when rGO was coated on the gold micropillars (Figure 3f and spectrum in Figure S3 (Supporting Information)). The existence of nitrogen for antigen immobilized sample (Figure 3f and spectra in Figure S3c (Supporting Information)) may come from the $-NH_2$ group of the protein (i.e., antigen). We note that the user interface for reading of the electrochemical cell signal was a laptop or a smartphone. A 3DcC device with a readout using a smartphone-based interface is shown in Figure 3g.

Cyclic voltammetry (CV) studies were carried out to investigate the electrochemical properties of the AJ-printed 3D Au electrode (i.e., with micropillar geometry shown in Figure 3) and compare it with AJ-printed 2D Au electrode (Figure S4, Supporting Information). The 3D Au (AJ-printed) and 2D Au (AJ-printed) electrodes showed clear oxidation and reduction peaks (Figure S4a, Supporting Information). The 3D Au electrode showed a 170% enhancement of current compared to the 2D Au electrode (Table S1, Supporting Information). This is due to larger-surface area and porous feature of the AJ printed 3D Au electrode. The 3D Au electrode provided both radial and linear diffusion of ions which enhanced the electrochemical current, while the planar 2D Au electrode provided only linear diffusion of the ions. This was confirmed by COMSOL simulations described in Figure S6 in the Supporting Information. After rGO coating, the electrochemical signal was decreased (Figure S4b, Supporting Information) due to the presence of functional groups on the rGO surface[27] that can hinder the electron transfer during the redox reaction. Further, the currents again decreased due to the immobilization of SARS-CoV-2 spike S1 antigens onto the two electrodes (Figure S4c, Supporting Information). To assess the mass transport of potassium ferro/ferricyanide, the scan rate studies were conducted (Figure S4d,e, Supporting Information). The variation of anodic

and cathodic peaks is plotted against the square root of scan rates (Figure S4f, Supporting Information) which indicates that these sensors showed a diffusion-controlled process. It is clear that the diffusion coefficient of 3D Au is 280% higher than 2D Au without rGO and antigens; 256% higher than 2D Au upon rGO coating; but reduced significantly upon loading of the antigen molecules. This study indicates that 3D geometry can hold higher amount of antigen molecules, thereby improving the sensor efficacy.

The electrodes were also characterized by the EIS method (Figure S5, Supporting Information) to investigate the electrode-electrolyte interfacial properties. The R_{ct} value of 3D Au electrode without any coating was 30 Ω (Figure S5a and Table S1, Supporting Information) possibly due to the highly conductive 3D microstructure and radial diffusion of the ions (Figure S6, Supporting Information). While rGO sheets are incorporated onto the 3D micropillar, the R_{ct} is increased to 0.894 kΩ (Table S1, Supporting Information) due to the presence of functional groups (COOH, OH) on rGO sheets. Further functionalization by SARS-CoV-2 spike S1 antigens on the 3D surface of rGO and Au increased the loading capacity of SARS-CoV-2 spike S1 antigen, leading to a maximum R_{ct} value of 3.51 kΩ. When compared to AJ-printed 2D Au electrodes (Figure S5b, Supporting Information), the AJ-printed 3D Au electrode (Figure S5a) showed a signal improvement of 330%. In phase-shift (θ) plots (Figure S5c,d, Supporting Information), the peak value of θ for AJ-printed 3D Au coated with rGO and antigens is found to be shifted to lower frequencies when compared to the AJ-printed 2D electrode.

In order to understand the electrochemical processes in the 3DcC device, we carried out simulations of the CV experiments using COMSOL Multiphysics Software for the 2D and 3D electrodes (Figure S6, Supporting Information). The bulk concentration was assumed to be 1 mol m^{-3}, while the diffusion coefficient was taken from that obtained in the experiments from the Randles–Sevcik equation.[25] Figure S6a in the Supporting Information shows the electrode geometry, while Figure S6b in the Supporting Information shows the diffusion profiles for a 10 × 10 array configuration. Figure S6c (Supporting Information) shows 2D and 3D electrodes with their planar, and spherical and planar diffusion profiles, respectively. The concentration of the diffusing species for array configurations of planar and 10 × 10 3D electrodes are shown in Figure S6d in the Supporting Information. The presence of radial diffusion as shown in COMSOL simulations confirms the speculation that this phenomenon may help create high redox current in case of the 3D electrodes.

We also conducted COMSOL simulations to investigate the effect of the AJ-printed electrode geometry/dimensions (Figure S1, Supporting Information, provides the variation in the electrode dimensions) on the current of the electrochemical cell. The model used for this simulation is the same as that described above and shown in Figure S6, Supporting Information. The simulation results are given in Figure S7 in the Supporting Information. The plots of currents versus applied potential are shown for various array configurations (Figure S7a, Supporting Information), pillar heights (Figure S7c, Supporting Information), and pillar diameters (Figure S7e, Supporting Information); while the corresponding currents are shown in Figure S7b,d,f in the Supporting Information, respectively. The experimental range of values for the pillar dimensions is also indicated in Figure S7b,d,f in the Supporting Information. It is clear that the electrochemical current is saturated at the array size of 10 × 10 (Figure S7a,b, Supporting Information). Further, the variations in the current for the experimental range of value is within ±2% for pillar height, ±1.0% for pillar diameter, ± 3.2% for pillar-to-pillar distance, which is reasonable.

SARS-CoV-2 S and N proteins have been used for serologic assays for detecting antibodies of SARS-CoV-2 infection.[10] The S protein binds to viral entry receptor angiotensin-converting enzyme-2 (ACE2) and mediates viral entry. It is present as a trimer with three receptor-binding S1 heads sitting on top of a trimeric membrane fusion S2 stalk.[28] The receptor-binding subunit S1 contains the N-terminal domain (NTD) and the RBD while the membrane fusion subunit S2 contains the fusion peptide (FP), two heptad repeats (HR1 and 2), a transmembrane anchor (TM) and the intracellular tail (IC).[28] Serologic assays using both recombinant S1 and RBD proteins have been shown to detect specific antibodies in COVID-19 patients.[29] For antibody tests in this work, we thus chose the spike S1 and RBD antigens of SARS-CoV-2 to develop the 3DcC testing platform.[30]

Figure 4 shows the impedimetric sensing plots and R_{ct} for the 3DcC sensor when the electrodes are exposed to phosphate buffer saline (pbs), rabbit serum (rs), fetal bovine serum (fbs), and spike S1 antibodies (rabbit IgG). The spike S1 antibodies were introduced successively at concentrations of 0.01×10^{-15} M, 1×10^{-15} M, 1×10^{-12} M, 100×10^{-12} M, 1×10^{-9} M, 10×10^{-9} M, and 30×10^{-9} M, three times each, wherein the sensor was regenerated after each set of measurements, including the controls testing. In the first set of measurements (**Figure 4**a), a testing baseline was set by allowing only the pbs solution with no target antibodies which showed a charge transferred-limited process with R_{ct} of 3.51 kΩ. While the sensor was tested with biological samples such as rs and fbs as controls, the sensor generated similar profiles of Nyquist plots having a deviation of ± 6.01% compared to the baseline signal. The adsorption of any proteins or albumins can change the sensor signals significantly. However, though these proteins have a major composition of albumin protein, the sensor did not show a significant change in the baseline signal. The sensor surface contained a layer of BSA molecules which are negatively charged, which may have repelled the albumin molecules in the serum due to their identical charge polarity.[31] This result indicated that the sensor was selective to specific proteins as was desired. With these control measurements, the 3DcC device was tested with low concentrations of spike S1 antibodies at 0.01×10^{-15} and 1×10^{-15} M. With the 0.01 fM concentration, a change of impedance signal (4.2 kΩ) was observed (Figure 4d) compared to the sensor baseline and the control serum. This is as expected since binding of the antibodies with the antigens will obstruct electron transfer from the electrolyte to the electrode surface resulting in an increase in circuit impedance as captured by the Nyquist plot. Between 0.01×10^{-15} and 1×10^{-15} M, the sensor did not show any significant change in impedance signal. Within this range of concentration of antibodies, the sensor surface may have only limited number of antibodies resulting in an unchanged signal. At 1×10^{-12} M concentration of antibodies, however,

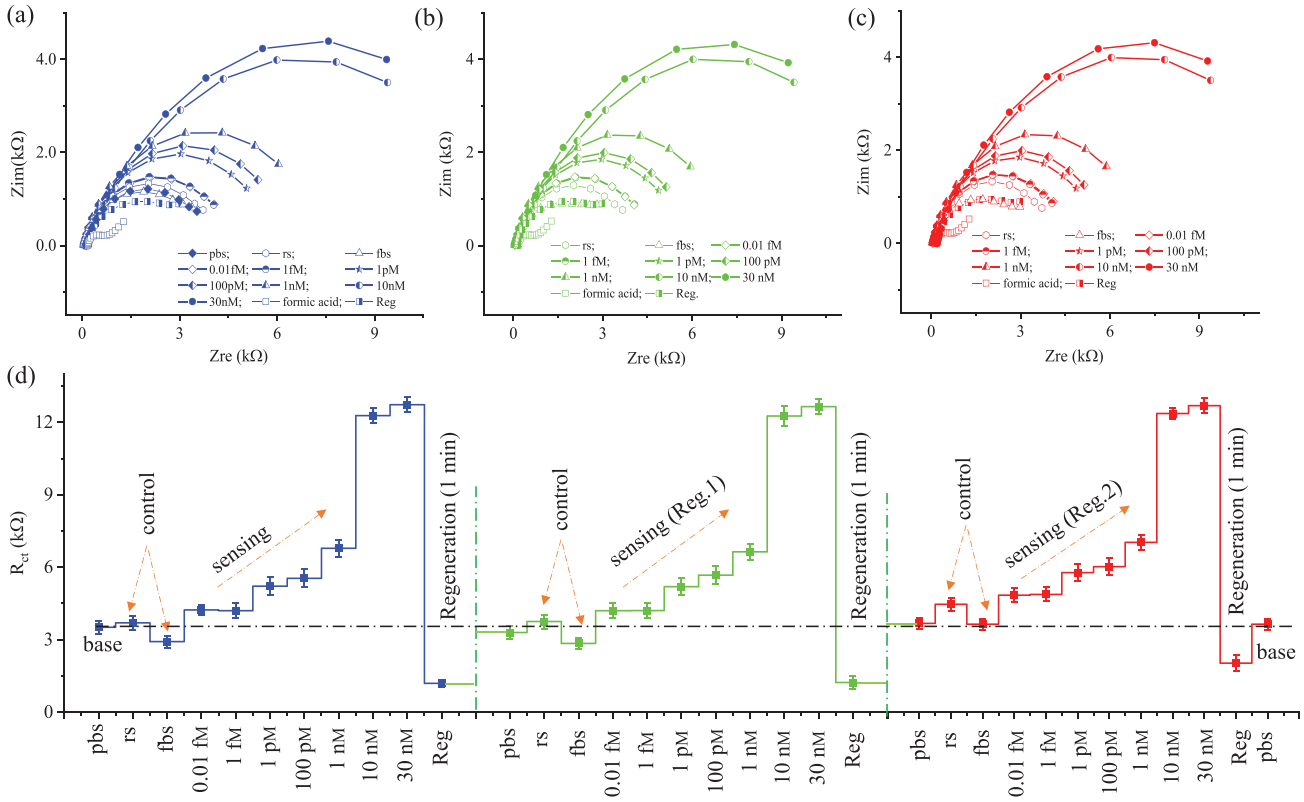

Figure 4. Sensing of antibodies to SARS-CoV-2 spike S1 antigen at different molar concentrations with regeneration. a) Nyquist plots of the 3DcC sensor measured by EIS method without and with the spike S1 antibodies at concentrations of 0.01×10^{-15} M, 1×10^{-15} M, 1×10^{-12} M, 100×10^{-12} M, 1×10^{-9} M, 10×10^{-9} M, and 30×10^{-9} M in pbs solution. b,c) Nyquist plots similar to that in (a) after two successive sensor regenerations by a low-pH chemistry consisting of 1.0 M (pH 2.5) formic acid solution. The regeneration was achieved within 60 s. For all concentrations, the signal in (b,c) was within 95% of that in (a). d) The charge transfer resistance (R_{ct}) for the 3DcC sensor for each concentration of antibodies and control serum before and after each regeneration for the data in (a–c). The fetal bovine serum (fbs) and rabbit serum (rs) in (a–d) were utilized as control biofluids. For all measurements, a 50×10^{-3} M pbs (pH 7.4) solution containing an equimolar concentration (5×10^{-3} M) of a ferro/ferricyanide mediator was used. Three successive readings were obtained at each concentration of the antibodies for the three data sets. Detection frequencies from 1 to 10 000 Hz were applied to obtain this data. There was no incubation time for all the measurements in this figure. The R_{ct} values in (d) were calculated by fitting the data in (a–c) to a Randles equivalent circuit shown in Figure 2e.

the sensor showed a significant increase in the impedance to 5.21 kΩ. As the antibody concentration was increased to 1×10^{-9} M, the R_{ct} increased further as reflected in the Nyquist plots. Interestingly, when a 10×10^{-9} M concentration was tested, the sensor provided a very significant increase in the impedance signal (12.3 kΩ). Further, a minor change of signal (12.7 kΩ) was observed at 30×10^{-9} M concentration. Testing beyond 10×10^{-9} M concentration of spike S1 antibodies showed that the sensor exhibited a saturated impedance signal, wherein the maximum number of binding sites on the sensor surface are likely to be occupied by the target antibodies.

To elute antibodies from the sensor surface, we exposed the sensor electrodes to a solution of formic acid (1.0 M) having a pH of 2.5. This was chosen as a pH of 2.5 is outside the physiological range for human body (7–7.4 pH), where antibodies are expected to elute from the antigens via a disruption of immunoaffinity.[32] Indeed, upon introduction of the formic acid solution for 60 s into the sensor, the R_{ct} values dropped to about 1.2 kΩ. In addition to eluting the antibodies, the low R_{ct} is caused by high electron transfer rates in acidic media. Note that the signal from formic acid in Figure 4a–c are after the 1st, 2nd, and 3rd regeneration. After the 60 s incubation by formic acid solution, the sensor was washed with pbs solution. At this point, the sensor recovered to 94% of its base signal. Figure 4b,c shows sets of measurements after regeneration for the same set of spike S1 antibody concentrations as studied in Figure 4a. After 1st regeneration, the signal with rb and fbs (Figure 4b) was within ±6.96% of the baseline. After 2nd regeneration, this signal did not change significantly (Figure 4c). We also observed similar patterns of impedance signals for spike S1 antibody solutions at different concentrations after 2nd regeneration as shown in Figure 4c,d. The spike S1 sensor could provide a low limit-of-detection (LoD) and an analytical sensitivity of 2.8×10^{-15} M, and 1×10^{-12} M respectively. Note that the LoD was calculated using reported literature[33] as shown in Section S1 in the Supporting Information. Two additional spike S1 sensors were also tested with serial dilution of antibodies and results are shown in Figure S8a–d in the Supporting Information.

Figure 5 shows the sensing of RBD antibodies using the 3DcC device where results are presented in a similar manner as that for spike S1 antibodies (Figure 4). The device had micropillar

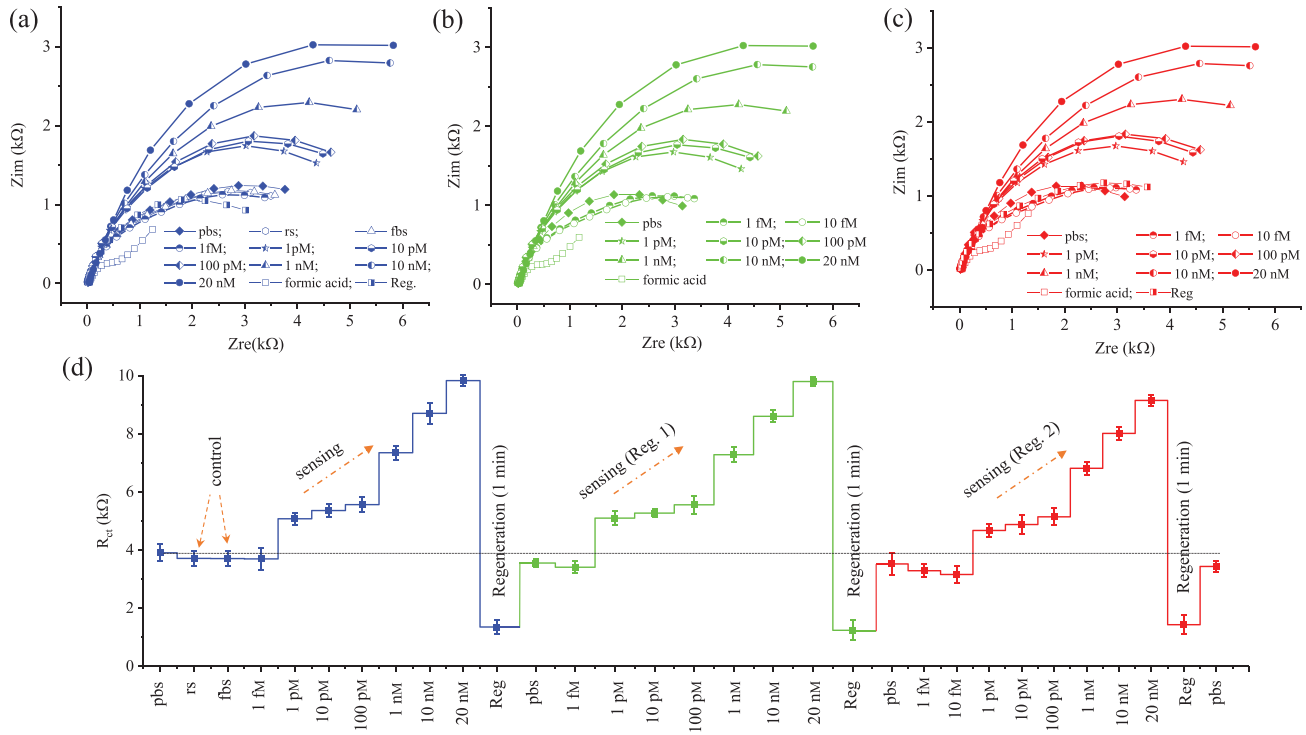

Figure 5. Sensing of antibodies to SARS-CoV-2 receptor binding domain (RBD) antigens at different molar concentrations with regeneration. a) Nyquist plots of the 3DcC sensor measured by EIS method without and with the RBD antibodies at concentrations of 1×10^{-15} M, 1×10^{-15} M, 1×10^{-12} M, 100×10^{-12} M, 1×10^{-9} M, 10×10^{-9} M, and 20×10^{-9} M in pbs solution. b,c) Nyquist plots similar to that in (a) after two successive sensor regenerations by a low pH chemistry consisting of 1.0 M (pH 2.5) formic acid solution. The regeneration was achieved within 60 s. For all concentrations, the signal in (b,c) was within 95% of that in (a). d) The charge transfer resistance (R_{ct}) for the 3DcC sensor for each concentration of antibodies and control serum before and after each regeneration for the data in (a–c). The fetal bovine serum (fbs) and rabbit serum (rs) in (a–d) were utilized as control biofluids. For all measurements, a 50×10^{-3} M pbs (pH 7.4) solution containing an equimolar concentration (5×10^{-3} M) of a ferro/ferricyanide mediator was used. Three successive readings were obtained at each concentration of the antibodies for the three data sets. Detection frequencies from 1 to 10 000 Hz were applied to obtain this data. There was no incubation time for all the measurements in this figure. The R_{ct} values in (d) were calculated by fitting the data in (a–c) to a Randles equivalent circuit shown in Figure 2e.

electrodes with immobilized SARS-CoV-2 RBD-His recombinant antigens. The EIS spectra for each concentration of RBD antibodies with control biofluids such as rs and fbs are shown in Figure 5a; while that after two successive regenerations are shown in Figure 5b,c. The RBD antibody concentrations were set from 1×10^{-15} M to 20×10^{-9} M to test the sensor. The sensor base signal was obtained by collecting impedance spectra in presence of pbs solution where the sensor showed a R_{ct} of 3.89 kΩ (Figure 5d). With the rs and fbs, the sensor showed a deviation of 3.0% in the impedance after regeneration when compared to sensor baseline. The sensor did not show any increased signal when 1.0×10^{-15} M concentration of RBD antibodies were introduced. At RBD antibody concentration of 1×10^{-12} M, the R_{ct} value changed to 5.07 kΩ. Similar to the spike S1 antibodies, as the concentration of RBD antibodies was increased from 1×10^{-12} M to 20×10^{-9} M, the R_{ct} values were found to increase as shown in Figure 5d. The regeneration of the RBD sensor was achieved by 1.0 M formic acid (pH 2.5) solution in 60 s; the same as that used for the regeneration of spike S1 antibodies. Unlike the spike S1 sensor, the RBD sensor showed different linear responses between 1×10^{-12} and 100×10^{-12} M, and 100×10^{-12} M to 20×10^{-9} M. After two regenerations, a minimum loss of sensitivity (± 1%) was observed for the RBD sensor. The RBD sensor could provide a low LoD and an analytical sensitivity of 16.9×10^{-15} and 1×10^{-15} M respectively (see Section S1 of Supporting Information for the calculation of LoD using reference[33]). Further, sensing data for two additional sensors of spike RBD antibodies are shown in Figure S8e–h in the Supporting Information. Based on the results in Figures 4 and 5, we created a dose-dependent response plot for spike S1 and RBD sensing, respectively, where a minimum R_{ct} value was identified above which the sensing could be achieved (Figure S9a,b in the Supporting Information).

We next discuss the detection time of the 3DcC sensor for spike S1 antibodies and RBD antibodies. **Figure 6**a show the impedance of the sensor as a function of time in seconds for the detection of spike S1 antibodies. It is noticed that without target in the pbs solution, the sensor impedance started to change at 3 s and reached to ≈1 kΩ in 10 s, beyond which it became saturated. When spike S1 antibodies (1×10^{-9} M) were introduced in six different sensors, a significant change of impedance was observed (in line with data in Figure 4) and reached about 93.2% of the saturation value in 11.5 s, indicating detection of antibodies. The magnitude of impedance at 11.5 s as a function of the spike S1 antibody concentrations (0.01×10^{-15} M to 30×10^{-9} M) for the 3DcC device is shown

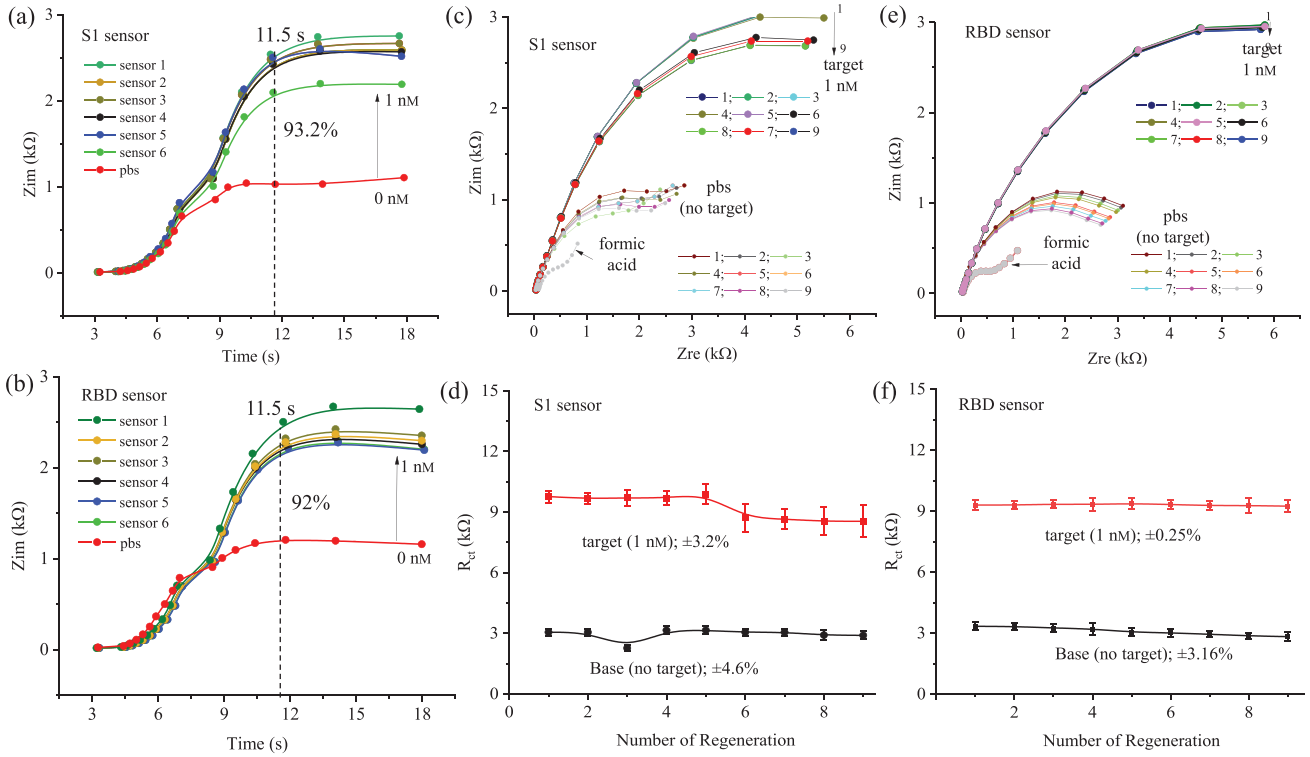

Figure 6. Detection time and regeneration studies of the 3DcC device. a,b) The detection time for spike S1 and RBD antibodies during the EIS measurements, respectively, for twelve different 3DcC devices. The device impedance is plotted against the detection time. The spike S1 and RBD sensors reached 93.2% and 92% of their saturation impedance at 11.5 s, respectively, allowing the signal detection in seconds. The concentration of antibodies was set to 1×10^{-9} M for this measurement. A frequency range of 1–10 000 Hz was used to obtain this data. The (Z_{im}) data is recorded from 3 s after the introduction of antibodies as the EIS measurement had to overcome the solution resistance, R_s, prior to obtaining the charge transfer resistance (see schematic in Figure 2e). c,d) Regeneration study showing Nyquist plots and charge transfer resistance for the detection of spike S1 antibodies for the 3DcC device. The regeneration is carried out 9 times. For each measurement, the sensor was first exposed to pbs, then to 1×10^{-9} M concentration of S1 antibodies in pbs, and finally to formic acid (1 M) with an incubation time of 60 s. The charge transfer resistance as a function of the number of regenerations is plotted in (d). e,f) Regeneration data for sensing of RBD antibodies by the 3DcC device. For both the sensors, a minimal loss in sensor performance is observed after nine regenerations.

in Figure S10a in the Supporting Information. The Figure 6b shows the impedance as a function of time for six different 3DcC RBD sensors when RBD antibodies are introduced at 1×10^{-9} M concentration. For all the sensors, the signal reached 92% of the saturation signal at 11.5 s, again indicating detection of the antibodies. Figure S10b in Supporting Information shows the time required to reach 95% of the saturation signal for the data presented in Figure 6a,b. The 3DcC device can thus detect the antibodies specific to SARS-CoV-2 within seconds, which is faster than any data yet reported in literature.

To validate the sensor regeneration phenomenon, 3DcC sensors for the detection of spike S1 antibody and RBD antibody were regenerated 9× each as shown in Figure 6c–f, respectively. A pbs solution was used as a reference while 1×10^{-9} M antibody solutions were used as the target. After 9× regenerations, the spike S1 and RBD sensors did not show significant changes in the R_{ct} values as evidenced by their low relative standard deviation (RSD) of less than ±3.2% and ±0.25%, respectively. However, the base line R_{ct} of spike S1 and RBD sensors was found to change by ±4.6% and ±3.1% when compared to that with no regeneration. We noted that even after 9 regenerations (i.e., 10th reading), both sensors provided a good signal, indicating a high regeneration capability. We speculate that acidic media may degrade the bonding between rGO and antigens after repeat exposures, possibly limiting the regeneration capability beyond a certain limit.

The sensitivities of the 3DcC device for spike S1 and RBD sensors are shown in Figure S10c,d in the Supporting Information. These plots are obtained from the R_{ct} values in Figures 4d and 5d. For spike S1 sensor, the slope of Figure S10c in the Supporting Information was 0.27 ± 0.04 kΩ per 10^{-9} M in the range of 1.0×10^{-15} M to 1×10^{-9} M, and 4.5 ± 1.1 kΩ per 10^{-9} M in the range of 1×10^{-9} to 30×10^{-9} M. The high sensitivity at higher concentrations is likely due to higher number of antibodies captured by the sensing surface. For the RBD sensor, the slope of Figure S10d in the Supporting Information was 0.39 ± 0.04 kΩ per 10^{-9} M for a range of 1.0×10^{-15} M to 0.1×10^{-9} M, and 1.7 ± 0.17 kΩ per 10^{-9} M for a range of 0.1×10^{-9} to 20×10^{-9} M. The spike S1 sensor showed a higher sensitivity at a higher concentration of antibodies when compared to the RBD sensor. We speculate that this high sensitivity of the 3DcC device was due to the 3D architecture, a high porosity, and specific surface chemistry that allowed an enhanced loading capacity of the antigens.

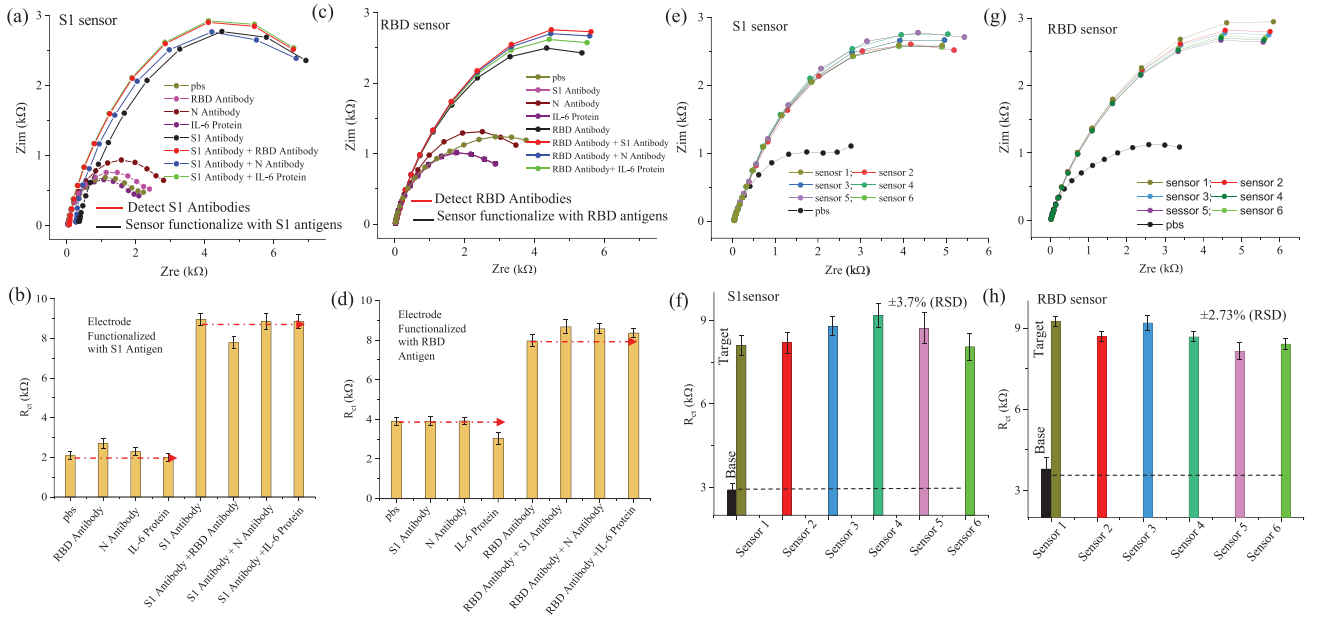

Figure 7. Cross-reactivity and reproducibility studies of the 3DcC device. a) Cross-reactivity test for the 3DcC device designed to detect spike S1 antibodies. Nyquist plots for the device are plotted for multiple antigens and antibodies in absence and presence of spike S1 antibodies. IL-6 or IL-6 antigen (0.05×10^{-9} M), nucleocapsid (N) antibody (1×10^{-9} M), and RBD antibody (0.1×10^{-9} M) are used for this measurement. b) The R_{ct} values were calculated from the Nyquist plots shown in (a). The 3DcC device provided minimal interference with other related proteins. c) Cross-reactivity test for the 3DcC device designed to detect RBD antibodies. Nyquist plots for the device are plotted for multiple antigens and antibodies in absence and presence of RBD antibodies. IL-6 antigen (0.05×10^{-9} M), N-antibody (1×10^{-9} M), and spike S1 antibody (0.1×10^{-9} M) are used for this measurement. d) The R_{ct} values were calculated from the Nyquist plots shown in (c). The 3DcC device provided minimal interference with other related proteins. e,f) The sensor reproducibility test on six different 3DcC sensors in presence of S1 antibodies (1×10^{-9} M in pbs). The sensor-to-sensor variation is evaluated by calculating the R_{ct} values for each sensor. This variation is within about 7%. The error bar is from at least three repeated measurements of the sensor. g,h) Reproducibility test data for sensing of RBD antibodies (1×10^{-9} M in pbs) from six different sensors. The sensor-to-sensor variation in this case is about 5%.

Figure 7a,b shows the Nyquist plots and R_{ct} for cross-reactivity study of the 3DcC sensor designed to test spike S1 antibodies, respectively. The sensor was tested in the presence of RBD antibodies, nucleocapsid (N) antibodies, and cytokines such as interleukin-6 (IL-6) antigens, without and with the spike S1 antibodies (1×10^{-9} M). In the absence of spike S1 antibodies, the sensor was found to be insensitive to N antibodies, RBD antibodies, and IL-6 protein molecules as evidenced by its low R_{ct} values and low RSD (±6.9%). The sensor showed a slight deviation (±6.5%) from the initial signal in the presence of RBD antibodies possibly due to the receptor similarity between the two antibodies. Alternatively, the RBD antibodies might recognize linear epitope while the S1 protein might have a specific confirmation that prevents binding to the RBD antibodies. The sensor was highly sensitive when the spike S1 antibodies were introduced with the above molecules, leading to an increase in the R_{ct} values shown in Figure 7b. Figure 7c,d shows the cross-reactivity studies of RBD antibodies. Again, we used N antibodies, IL-6 antigens, and spike S1 antibodies in the absence and presence of RBD antigens (1×10^{-9} M). In this result, the 3DcC device tested with IL-6 antigen showed a deviation of ±11.0% compared to base line with no target. We note that the decrease of R_{ct} value with IL-6 antigen did not affect the sensor response when target antibodies were present in the buffer solution. Without RBD antibodies, the 3D sensor showed an RSD of ± 5.81% compared to baseline signal while the RSD was reduced to ± 2% in the presence of 1×10^{-9} M target RBD antibodies. It is clear that specific binding sites on the antigen molecules (epitope) reject binding by non-specific molecules but allow binding to a specific antibody (paratope). These results indicated that the sensor showed a good selectivity even within a similar group of proteins.

We next show the sensor reproducibility (Figures 7e–h) where twelve 3DcC sensors, 6 for spike S1 antibodies and 6 for RDB antibodies were evaluated. Nyquist plots were obtained and R_{ct} values were calculated at fixed concentration (1×10^{-9} M) of spike S1 (Figures 7e,f) and RBD (Figure 7g,h) antibodies. For spike S1 and RBD antibodies, the sensors showed a RSD of ± 3.7% and ± 2.7%, respectively, indicating reasonable reproducibility of the sensor. Note that additive manufacturing (AM) processes are digital (i.e., controlled by CAD programs) and hence are expected to be repeatable (Figure S1, Supporting Information). However, all AM processes are known to have microstructural inhomogeneities in their final parts.[34] It is clear that for the 3DcC device, the AJ nanoparticle printing process created repeatable structures (Figure 3b; Figure S2a, Supporting Information) that provided acceptable repeatability in antibody sensing performance (Figure 7e–h), but led to a microstructure on the pillar surface (high-magnification images of Figure 3c and Figure S2a (Supporting Information)) that aided in the surface functionalization process.

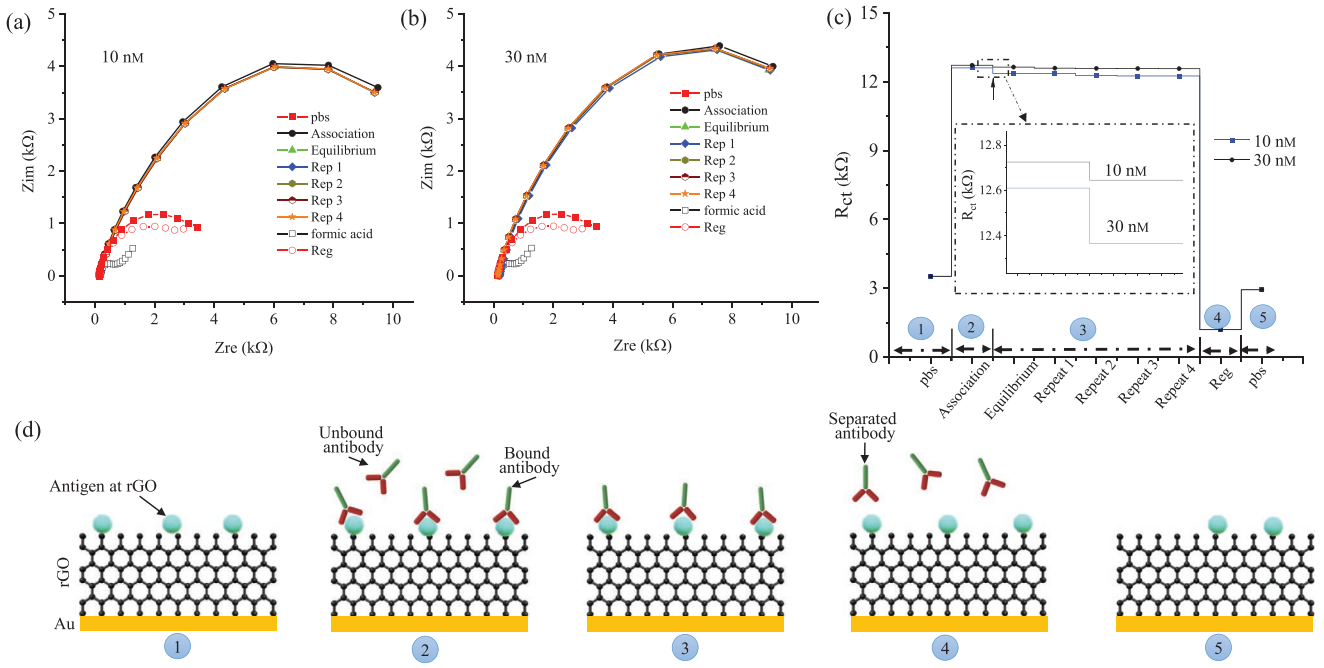

Figure 8. Study of the kinetics of antigen–antibody interactions. a) Nyquist plots for spike S1 antibodies at concentrations of 10×10^{-9} M (a) and 30×10^{-9} M (b) at the micropillar surface showing their association, equilibrium, and regeneration phases. c) Variation in the R_{ct} values during antigen–antibody interaction for spike S1 antibodies at 10×10^{-9} and 30×10^{-9} M concentrations. Repeat 1, 2, 3, and 4 are the replicate plots in the equilibrium phase. d) Schematic of the association, equilibrium, and regeneration of the kinetics shown in (a), (b), and (c). In association phase, the target antibodies (10×10^{-9} and 30×10^{-9} M) with buffer solution are loaded into the 3DcC device. The antibodies attach to the antigens. However, some unbound antibodies may be present in the solution near the sensor surface and contribute to the R_{ct}. In equilibrium phase, fresh pbs (without antibodies) is used to wash the 3DcC device, thus removing the unbound antibodies in the solution, and reducing the R_{ct} slightly. In the regeneration phase, a solution of formic acid (1 M; pH 2.5) is used to regenerate the sensor surface, thus eluting the antibodies from the antigens and lowering R_{ct} significantly.

We also investigated the real-time tracking of binding kinetics of antigens and antibodies at the sensor surface. **Figure 8**a–d show impedance graphs, R_{ct} values, and a schematic explaining the various phases of binding events such as association, equilibrium, and regeneration, respectively. In the association phase, the sensor is exposed to a concentration of target antibodies (spike S1 in this case) where both bound and unbound molecules were present resulting in a slightly higher R_{ct} (Figure 8a,b). In the equilibrium phase, the sensor was washed by buffer solution and unbound antibodies were removed from the sensor resulting in a slight reduction in the R_{ct}. However, during regeneration by a low-pH chemistry, elution or desorption of antibodies from the antigens occurred via disruption of ionic and hydrogen bonds in the immunocomplex,[35] reducing the R_{ct}. The signal change from association to equilibrium phase is relatively low. This may be due to the static measurement conditions in our experiments where the buffer solution is stagnant rather than having an active circulation. The signal is relatively stable over time as shown in the repeatable measurements. A similar result was obtained when two addition sensors for sensing of RBD antibodies were tested (Figure S11, Supporting Information).

The AJ-nanoprinted platform (i.e., 3DcC device) developed in this work can detect antibodies for SARS-CoV-2 within seconds. The research also represents an important advance in the use of nanomaterials and nanofabrication methods in realizing rapid detection of pathogenic biomarkers at low concentrations.

The 3DcC device (Figure 3), which includes the WE with micropillar geometry with surface porosity and a chemistry involving flaky rGO (Figure 3; Figure S2, Supporting Information) allowed a high redox current for the electrochemical cell forming the sensor (Figure S4, Supporting Information). Further, the 3D geometry allowed a relatively high loading of biorecognition elements (antigens) for the sensor, enabling the detection of the antibodies with LoDs of 2.8×10^{-15} and 16.9×10^{-15} M for spike S1 and RBD antibodies (Section S1, Supporting Information), respectively. Figure 7a–d demonstrates that the natural construction of antigen–antibody immunocomplex makes sensing selective. Another important outcome of this work is the regeneration of the sensor in one minute. By introducing formic acid with a pH of 2.5, which is outside of the physiological range observed in the body (7–7.4), the antibodies were eluted from the antigens allowing full recovery of the original sensor signal. The demonstration of 10 repetitions (9× regenerations) of the sensors for each of the antibodies (Figure 6c–f) gives the opportunity for the same sensor to be used multiple times in the field without losing the specificity and sensitivity. We also note that the 3DcC requires only a few micromolar of fluid for detection of antibodies (e.g., volume obtained by a finger prick with appropriate dilution). Lastly, a convenient smartphone-based user interface (Figure 3g) will

enhance testing accessibility of the device in underdeveloped areas.

We point to several advantages offered by the nanomaterial-based construction of the device. The surface features (Figure 3c; Figure S2a, Supporting Information) of the gold pillars are a result of the AJ-nanoprinting process and allow an excellent coverage of the rGO on the electrode surface (e.g., rGO may not be coated on a smooth gold surface). In addition, rGO nanoflakes form a secondary 3D structure (Figure S2b, Supporting Information), allowing high loading of the antigens. We also note that the EDC:NHS chemistry used in the work covalently binds the $-COOH$ group of rGO to $-NH_2$ group of antigens, which is common to several proteins. It is thus feasible to immobilize antibodies on the sensor surface and detect pathogens directly via their antigens. The AJ nanoprinting is a digital manufacturing platform where the sensor design is controlled by CAD programs. The fabrication is also rapid – the 10×10 gold pillar array (Figure 2b) takes 35 min to print per printhead. With the availability of AJ printers with four printheads working in tandem, the effective printing time can be reduced to 7–8 min per sensor followed by a batch sintering process. Such digital manufacture allows fabrication in two simple steps without the need for any cleanroom processes, lowering resources/cost per sensor that can improve accessibility of testing. In addition, 3D printing enables the sensor design to be changed via simple changes to CAD programs. A multiplexed chip where several working electrodes are printed on the same device can allow selective immobilization of several antigens of SARS-CoV-2 to detect multiple antibodies at the same time. Such a device can improve fidelity of detection and also allow the same device to be used for multiple tests. Such work will be part of a future investigation.

The 3DcC device has several advantages over other methods for COVID-19 detection. Genomic sequencing, CRISPR-based test, and RT-qPCR[5,6] are accurate but have a long testing time (days). Other methods such as ELISA and lateral flow measurements are less sensitive and cannot provide diagnostic information within seconds at high accuracies.[10] The 3DcC device, however, has the ability to detect SARS-CoV-2 antibodies non-destructively within seconds at low analytical sensitivities with label-free probing of antibodies and an ability for regeneration within one minute. These results are highly encouraging and a device for field use, after appropriate human trials, will have a significant positive impact on public health and the course of the current[36] as well as future pandemics. Note that we obtained a signal in all the 3DcC devices used in this research every time when an antibody solution was introduced (Figures 4–8). Although this is a very good initial indicator, studies with large scale patient samples to evaluate the sensitivity and specificity are necessary in order to establish statistical rates for false negatives and false positives. We also note that the concentration of antibodies to SARS-CoV-2 in body fluids of COVID-19 patients likely varies significantly (e.g., for asymptotic versus symptomatic patients) and has not been investigated at this time. However, LoD at femtomolar concentrations for antibodies may enable an early detection of the disease which needs to be investigated urgently.

In summary, we have developed a nanomaterial-based advanced biosensing platform to detect antibodies specific to SARS-CoV-2 within seconds. The device is fabricated by using Aerosol Jet nanoparticle 3D-printing method to create gold micropillar array electrodes, followed by functionalization of rGO nanoflakes and immobilization of antigens on the electrode surface using an EDC:NHS chemistry. The detection of antibodies was achieved by electrochemical transduction when antibodies introduced in a fluid formed an immunocomplex with antigens on the 3D electrode surface. This signal was highly selective and repeatable. Antibodies to spike S1 and RBD antigens of the virus were detected at an analytical sensitivity of 1×10^{-12} M and 1×10^{-15} M, respectively. A low pH chemistry was used to regenerate the sensor via elution of antibody–antigen immunoaffinity within 1 min, allowing up to ten successive readings from the same sensor with high fidelity. This biosensing platform will allow rapid detection and early isolation of infection, saving lives. The test platform is generic and can potentially be used to detect biomarkers for other pathogens such as Zika virus, Ebola virus, and HIV. Finally, the platform will provide a powerful tool to investigate the dynamics of immune response during infections and after recovery.

Experimental Section

Materials: To construct the 3D array electrode using AJ printing, a commercial gold (Au) nanoparticle ink (UTDAu40, UT Dots Inc., Champaign, IL, USA) was used. The Au particle size was 2–5 nm, the ink viscosity was 3 cP, and particle loading in the ink was 40 wt%. The Au nanoparticles were dispersed in an organic non-polar solvent, which was aerosolized during AJ printing via ultrasound energy. The PDMS (SYLGARD 184 Silicone Elastomer Kit, Dow Corning, Midland, MI, USA) with a base to hardener ratio of 10:1 was used to create the microfluidic channel of the 3DcC device.

Human recombinant SARS-CoV-2 spike S1-His protein (50 μg mL^{-1}) and SARS-CoV-2 spike RBD-His protein (50 μg mL^{-1}) expressed in HEK293 cells, were the antigens purchased from the Sino Biological US Inc., Wayne, PA, USA. Before immobilizing on the 3D electrode surface, both the antigens were diluted to 5 μg mL^{-1} using the carbonate buffer solution (pH ≈ 9.6). Two rabbit IgG antibodies, SARS-CoV-2 spike S1 antibody (10 μL), and SARS-CoV-2 spike RBD antibody (10 μL) were also obtained from Sino Biological US Inc., Wayne, PA, USA. Both the antibodies were diluted in phosphate buffer saline solution (pH 7.4) containing a 5×10^{-3} M ferro/ferricyanide before their introduction into the microfluidic channel for measurements. These solutions were stored at –20 °C before their use. Mouse monoclonal antibody (MAb) of human recombinant SARS-CoV-2 nucleoprotein (N- protein) (Cat. No. 40143-MM05) was purchased from Sino Biological Inc., Wayne, PA. *E. coli* derived human recombinant IL-6 (Cat. No., 206-IL) antigen was purchased from R&D Systems, Inc., Minneapolis, MN, USA. Bovine serum albumin (BSA), sodium bicarbonate, sodium carbonate, formic acid, phosphate buffered saline tablet, EDC (1-ethyl-3-(3-dimethylaminopropyl) carbodiimide hydrochloride) and NHS (*N*-hydroxysuccinimide) were acquired from Sigma Aldrich, St. Louis, MO, USA. A room temperature curable silver/graphene conductive epoxy (type G6E-RTSG, Graphene Supermarket, Inc., Ronkonkoma, NY, USA) was used to connect wires to the pads of WE, CE, and RE (Figure 1) of the 3DcC device.

Fabrication of Electrodes for 3DcC Device: Figure 1 shows the fabrication process of the 3DcC device for rapid detection of COVID-19 antibodies. First, a patterned Au layer (with Cr adhesion layer) was deposited on a glass slide (Figure 1a) which formed the base for the three electrodes, namely, RE, WE, and CE. To pattern Au/Cr layer, a shadow mask was created using a Kapton tape which was cut using an automated cutter (Silhouette Curio, Silhouette America, Inc., Lindon, UT, USA) with the

aid of AutoCAD software (AutoCAD 2015, Autodesk Inc., San Rafael, CA, USA). A 5 nm thick Cr layer was deposited as an adhesive layer, followed by a 100 nm thick Au layer using an e-beam evaporator (Kurt Lesker PVD 75, Jefferson Hills, PA, USA) while using the Kapton shadow mask. The area of the patterned WE was 2 mm × 2 mm. Aerosol Jet nanoparticle 3D printing was then used to fabricate the 3D micropillar electrode on the WE as shown in Figure 1b–d.

The schematic of the AJ 3D printer (Model AJ-300, Optomec, Inc., Albuquerque, NM, USA) is shown in Figure 1b. The AJ printer consisted of an ultrasound atomizer, a deposition head with a nozzle, a movable (X-Y direction) platen with temperature control, and a shutter to break the flow of the aerosol as necessary. The ultrasonic atomizer created a mist of aerosol droplets of about 1–5 µm diameter from the Au ink, with each droplet containing the Au particles. A carrier gas (N_2) transported the droplets to the nozzle of the deposition head, while a sheath gas (also N_2) helped focus the nanoparticle beam to a length scale of 10 µm. The carrier gas pressure was set to be about 24 sccm and sheath gas pressure to set to 60 sccm. The nozzle diameter used for printing was 150 µm. Before printing, the geometry of the micropillar array was drawn in AutoCAD using a program in the software AutoLISP (AutoCAD 2015, Autodesk Inc., San Rafael, CA, USA) and converted to a "prg" file compatible with the AJ printer software. One milliliter gold nanoparticle ink without any dilution was loaded inside a glass vial (Figure 1b), atomized using ultrasonic energy, and transported to the AJ printer. An external heating element was placed on top of the *X–Y* stage to heat the substrate to 150 °C. A layer-by-layer printing sequence was used to build up the 3D 10 × 10 micropillar arrays from AJ droplets where the path of the droplets could be periodically blocked (or cleared) by controlling the shutter. The schematic of complete micropillar array is shown in Figure 1c. The printing of an individual pillar is shown in Figure 1d, where a layer of droplets was deposited on top of the previously printed and solidified Au micropillars. The strong surface tension of the printed ink caused the pillar to form without any support structures (Figure 1d). The printing process for the 10 × 10 micropillar array was completed within 35 min for a given printhead. After printing, the dried micropillar array was sintered at 400 °C for 5 h to completely remove the binders and sinter the Au nanoparticles which completed the manufacture of the WE of the device.

The surface of the RE on the glass substrate (Figure 1a) was then coated with commercial silver/silver chloride ink (Ercon, Inc. Wareham, MA, USA) by placing a Kapton shadow mask. The curing temperature for this coat was 150 °C for 2 h. The ink composition comprised of dispersed chloridised silver flake particulates in a solvent. Compared to thin film Ag/AgCl reference electrode, the commercial ink was chosen due to its improved stability as demonstrated in literature.[37]

The process of functionalization of WE are shown in Figure 2. First, the gold micropillars were functionalized with rGO (Figure 2a,b). The rGO nanoflakes (i.e., sheets) were obtained in powder form (CAS-No. 7782-42-5, ACS Materials LLC, Pasadena, CA, USA). The rGO sheets were dispersed in DI water (0.2 mg mL^{-1}) and sonicated for 2 h. As per the manufacturer, the rGO was obtained from graphene using a reduction process based on hydrazine (N_2H_4) treatment. Per the manufacturer data sheet, the rGO sheets had a conductivity >500 S m^{-1}, a diameter 0.5–10 µm, and a thickness ≈1 nm. Before coating, a PDMS fence was created and placed surrounding the Au micropillar array. A 20 µL rGO solution was drop-cast onto the Au micropillar array using a pipette and dried at 80 °C for an hour. This process was repeated three times. Though we did not expect the coating to be uniform, the Au pillars were covered by rGO sheets as observed in the SEM images (Figure 3d; Figure S2b,c in the Supporting Information) and Raman analysis (Figure 3e). The Au micropillar–rGO surface was further functionalized using SARS-CoV-2 antigens (Figure 2c). This was achieved by using a coupling reagent consisting of a mixture of EDC (0.2 M) and NHS (0.05 M) in ratios 1:1 by volume. A 20 µL solution of the EDC:NHS mixture was spread over the rGO–Au surface to activate —COOH groups of the rGO sheets. The electrode on the glass substrate was kept in a humid chamber (≈100% of humidity) for four hours and washed with pbs solution. Next, a 20 µL of SARS-CoV-2 spike S1 antigen solution (5 µg mL^{-1}) was spread on the surface of the rGO–Au array electrode via drop-casting using a pipette (10–50 µL; Cole-Parmer; Vernon Hills, IL, USA) and kept for 4 h in a humid chamber, followed by washing with pbs and storing in a refrigerator (4 °C) before its use. The activation achieved by EDC:NHS chemistry enabled the primary amine ($—NH_2$) groups of the protein molecules (i.e., antigens) of SARS-CoV-2 spike to form C—N bonds with the —COOH groups of rGO sheets via an amidation reaction. In this reaction, the EDC is known to act as a cross-linker and NHS as an activator.[24] Another SARS-CoV-2 antigen called spike RBD, was also immobilized on different sensors using same mechanism as that described above. For the RBD antigen, a 20 µL solution (5 µg mL^{-1}) was used for drop-casting over the Au micropillar–rGO electrode. For all sensors, a 20 µL of BSA solution (2 mg mL^{-1}) was introduced to the WE surface to block any non-specific sites of the antigen conjugated rGO–Au pillar. In this device, the 3D electrodes acted as sensitive immuno-detectors for COVID-19 antibodies without any labelling agents via antibody–antigen interactions (Figure 2d).

Fabrication of PDMS Housing and Assembly of the 3DcC Device: The PDMS housing of the 3DcC device was fabricated by soft-replica molding method (Figure 1e) and integrated with the glass containing functional electrodes (Figure 1f). A thick PMMA mold was created using high-precision milling machine that had a channel with 1 mm depth, 2 mm width, and 2 cm length. The channel width in the middle 1 cm section was increased to 2 mm (Figure 1e, Step 1). A PDMS solution was poured on the PMMA channel to copy an opposite pattern (Figure 1e, Step2). The bubbles were removed from liquid PDMS mixer by degassing for 1 hour in a vacuum chamber (10^{-4} Torr). Curing temperature was 80 °C for 2 h. The PDMS substrate was peeled off from PMMA channel (Figure 1e, Step 2) and acted a master reverse-mold for creating the final microfluidic channel. The surface of this PDMS mold was treated with silicone oil (Ease Release 205, Reynoldsam Advanced Materials, Macungie, PA, USA). A new mixer solution of PDMS was then poured into the PDMS mold (Figure 1e, Step 3) and then peeled off, resulting in the PDMS channel required for the 3DcC device (Figure 1e, Step 4). Holes were then punched at two ends of the channels by a hollow needle and tygon tubes were inserted for fluid injection. Finally, the PDMS slab was manually placed on the glass substrate such that the CE, WE, and RE were under the channel. Wires were connected to the pads of the electrode outside the PDMS channel using a room temperature curable silver/graphene conductive epoxy to connect to a potentiostat. A syringe was used to inject the testing fluid into the sensor in about 2 s. The volume of the entire microfluidic channel used for this study was 30 mm^3, requiring 30 µL of fluid with the antibodies.

Electrode Characterization: An electrochemical workstation with Zview software (VersaSTAT 3 Potentiostat Galvanostat, Princeton Applied Research, Oak Ridge, TN, USA) were used to record the electrochemical signals and analyze the impedance spectra. In addition, we also enabled a smartphone-based reading platform where the sensor was interfaced with an Android mobile phone using a portable device (Sensit Smart Device, PalmSens, Inc., Randhoeve 221, GA Houten, The Netherlands). The Sensit Smart is a microcontroller-based system having a tiny (30.5 mm × 18 mm × 2.6 mm) system-on-module (SOM) potentiostat. The potentiostat device could be directly connected to smart phone via a USB-C interface. Further, a mobile app "PStouch" was used to record the data. The Au micropillar electrodes were imaged by a scanning electron microscope (FEI Sirion SEM, Hillsboro, OR, USA). The elemental analysis was carried out using EDX in the same instrument as the SEM imaging. The Raman spectra were collected using the NT-MDT AFM/Raman (NT-MDT America, Tempe, AZ, USA) that used a 532 nm green laser with 12 mW laser power for excitation.

Electrochemical Simulations: The modeling and (3D simulation) of the different electrode structures was conducted using finite element software, COMSOL Multiphysics (Version 5.5, COMSOL Inc., Burlington, MA, USA). This study was carried out to investigate the diffusion profiles for different geometries of the electrodes and their corresponding electrochemical currents which were generated due to an electrochemical reaction at the surface of the electrode (Figure S6, Supporting Information). In this electroanalysis scheme, a redox species

B was considered to be oxidized to form a product (A) by losing an electron ($B \leftrightarrow A + e^-$). At the boundary, the product concentration was zero, but the bulk concentration of oxidative species was taken to be 1 mol m^{-3} and uniform. In this study, Fick's second law of diffusion was utilized as the domain equation which is given as $\frac{\partial c_i}{\partial t} = \nabla.(D_i.\nabla c_i)$, wherein the $c_i = 1$ mol m^{-3}. The diffusivities were taken for the 2D and 3D electrodes as obtained from the cyclic voltammograms at different scan rates, along with the Randles–Sevcik equation (Figure S6b,c, Supporting Information).[38]

Supporting Information

Supporting Information is available from the Wiley Online Library or from the author.

Acknowledgements

The authors acknowledge use of the materials characterization facility at Carnegie Mellon University supported by grant MCF-677785 for SEM and Raman Spectroscopy. All data needed to evaluate the conclusions in the paper are present in the paper and/or the Supplementary Materials. Additional data related to this paper may be requested from the authors.

Conflict of Interest

The authors declare no conflict of interest.

Author Contributions

R.P. came up with the concept and directed the research. A.A. built the device, developed the various chemistries required for functioning of the device, carried out all the tests, and wrote the first draft of the manuscript. S.J.G. and E.J. provided inputs from biology side and provided several biomolecules used in this research. C.H. and B.Y. carried out the AJ printing of the Au micropillar electrodes. M.S.S. wrote the original program for AJ printing of micropillars. S.J. carried out SEM microscopy, EDX analysis, and Raman studies, along with the simulations of the electrochemical process using COMSOL software. All authors contributed to interpreting the data and preparing and editing the manuscript.

Keywords

3D printing, 3D sensors, antibody tests, COVID-19, gold nanoparticles, micropillars, pandemics, reduced graphene oxide

Received: September 30, 2020
Revised: November 11, 2020
Published online: December 22, 2020

[1] a) L. Ferretti, C. Wymant, M. Kendall, L. Zhao, A. Nurtay, L. Abeler-Dörner, M. Parker, D. Bonsall, C. Fraser, *Science* **2020**, *368*, eabb6936; b) P. Zhou, X.-L. Yang, X.-G. Wang, B. Hu, L. Zhang, W. Zhang, H.-R. Si, Y. Zhu, B. Li, C.-L. Huang, *Nature* **2020**, *579*, 270.

[2] D. S. Hui, E. I. Azhar, T. A. Madani, F. Ntoumi, R. Kock, O. Dar, G. Ippolito, T. D. Mchugh, Z. A. Memish, C. Drosten, *Int. J. Infect. Dis.* **2020**, *91*, 264.

[3] a) M. Qin, Z. Cao, J. Wen, Q. Yu, C. Liu, F. Wang, J. Zhang, F. Yang, Y. Li, G. Fishbein, S. Yan, B. Xu, Y. Hou, Z. Ning, K. Nie, N. Jiang, Z. Liu, J. Wu, Y. Yu, H. Li, H. Zheng, J. Li, W. Jin, S. Pang, S. Wang, J. Chen, Z. Gan, Z. He, Y. Lu, *Adv. Mater.* **2020**, *32*, 2004901; b) S. Peng, F. Cao, Y. Xia, X. D. Gao, L. Dai, J. Yan, G. Ma, *Adv. Mater.* **2020**, *32*, 2004210.

[4] M. Gatto, E. Bertuzzo, L. Mari, S. Miccoli, L. Carraro, R. Casagrandi, A. Rinaldo, *Proc. Natl. Acad. Sci.* **2020**, *117*, 10484.

[5] J. P. Broughton, X. Deng, G. Yu, C. L. Fasching, V. Servellita, J. Singh, X. Miao, J. A. Streithorst, A. Granados, A. Sotomayor-Gonzalez, K. Zorn, A. Gopez, E. Hsu, W. Gu, S. Miller, C.-Y. Pan, H. Guevara, D. A. Wadford, J. S. Chen, C. Y. Chiu, *Nat. Biotechnol.* **2020**, *38*, 870.

[6] a) N. Zhu, D. Zhang, W. Wang, X. Li, B. Yang, J. Song, X. Zhao, B. Huang, W. Shi, R. Lu, *N. Engl. J. Med.* **2020**, *382*, *727*; b) V. M. Corman, O. Landt, M. Kaiser, R. Molenkamp, A. Meijer, D. K. Chu, T. Bleicker, S. Brünink, J. Schneider, M. L. Schmidt, *Eurosurveillance* **2020**, *25*, 2000045.

[7] G. M. Bwire, M. V. Majigo, B. J. Njiro, A. Mawazo, *J. Med. Virol.*, https://doi.org/10.1002/jmv.26349.

[8] M. Shen, Y. Zhou, J. Ye, A. A. A. Al-Maskri, Y. Kang, S. Zeng, S. Cai, *J. Pharm. Anal.* **2020**, *10*, 97.

[9] M. Riccò, P. Ferraro, G. Gualerzi, S. Ranzieri, B. M. Henry, Y. B. Said, N. V. Pyatigorskaya, E. Nevolina, J. Wu, N. L. Bragazzi, *J. Clin. Med.* **2020**, *9*, 1515.

[10] a) Z. Li, Y. Yi, X. Luo, N. Xiong, Y. Liu, S. Li, R. Sun, Y. Wang, B. Hu, W. Chen, *J. Med. Virol.* **2020**, *92*, 1518; b) L. Guo, L. Ren, S. Yang, M. Xiao, D. Chang, F. Yang, C. S. Dela Cruz, Y. Wang, C. Wu, Y. Xiao, *Clin. Infect. Dis.* **2020**, *71*, 778.

[11] J. Bedford, D. Enria, J. Giesecke, D. L. Heymann, C. Ihekweazu, G. Kobinger, H. C. Lane, Z. Memish, M.-d. Oh, A. Schuchat, *Lancet* **2020**, *395*, 1015.

[12] L. Xu, D. Li, S. Ramadan, Y. Li, N. Klein, *Biosens. Bioelectron.* **2020**, *170*, 112673.

[13] Y. Pan, X. Li, G. Yang, J. Fan, Y. Tang, J. Zhao, X. Long, S. Guo, Z. Zhao, Y. Liu, H. Hu, H. Xue, Y. Li, *J. Infect.* **2020**, *81*, e28.

[14] a) M. Yuan, H. Liu, N. C. Wu, C.-C. D. Lee, X. Zhu, F. Zhao, D. Huang, W. Yu, Y. Hua, H. Tien, *Science* **2020**, *369*, 1119; b) B. Ju, Q. Zhang, J. Ge, R. Wang, J. Sun, X. Ge, J. Yu, S. Shan, B. Zhou, S. Song, X. Tang, J. Yu, J. Lan, J. Yuan, H. Wang, J. Zhao, S. Zhang, Y. Wang, X. Shi, L. Liu, J. Zhao, X. Wang, Z. Zhang, L. Zhang, *Nature* **2020**, *584*, 115.

[15] Q.-x. Long, H.-j. Deng, J. Chen, J. Hu, B.-z. Liu, P. Liao, Y. Lin, L.-h. Yu, Z. Mo, Y.-y. Xu, F. Gong, G.-c. Wu, X.-x. Zhang, Y.-k. Chen, Z.-j. Li, K. Wang, X.-l. Zhang, W.-g. Tian, C.-c. Niu, Q.-j. Yang, J.-l. Xiang, H.-x. Du, H.-w. Liu, C.-h. Lang, X.-H. Luo, S.-b. Wu, X.-p. Cui, Z. Zhou, J. Wang, C.-j. Xue, X.-f. Li, L. Wang, X.-j. Tang, Y. Zhang, J.-f. Qiu, X.-m. Liu, J.-j. Li, D.-c. Zhang, F. Zhang, X.-f. Cai, D.-q. Wang, Y. Hu, J.-h. Ren, N. Tang, P. Liu, Q. Li, A.-l. Huang, *medRxiv* **2020**, https://doi.org/10.1101/2020.03.18.20038018.

[16] A. Petherick, *Lancet* **2020**, *395*, 1101.

[17] M. R. de Eguilaz, L. R. Cumba, R. J. Forster, *Electrochem. Commun.* **2020**, *116*, 106762.

[18] Z. Gao, Y. Li, X. Zhang, J. Feng, L. Kong, P. Wang, Z. Chen, Y. Dong, Q. Wei, *Biosens. Bioelectron.* **2018**, *102*, 189.

[19] S. Saliterman, *Fundamentals of BioMEMS and Medical Microdevices*, Vol. *153*, SPIE Press, Bellingham, WA, USA **2006**.

[20] K. Hong, Y. H. Kim, S. H. Kim, W. Xie, W. D. Xu, C. H. Kim, C. D. Frisbie, *Adv. Mater.* **2014**, *26*, 7032.

[21] H. Yang, M. T. Rahman, D. Du, R. Panat, Y. Lin, *Sens. Actuators, B* **2016**, *230*, 600.

[22] M. S. Saleh, C. Hu, R. Panat, *Sci. Adv.* **2017**, *3*, e1601986.

[23] a) J. S. Y. Chia, M. T. Tan, P. S. Khiew, J. K. Chin, C. W. Siong, *Sens. Actuators, B* **2015**, *210*, 558; b) K. Erickson, R. Erni, Z. Lee, N. Alem, W. Gannett, A. Zettl, *Adv. Mater.* **2010**, *22*, 4467.

[24] E. Y. Liu, S. Jung, D. A. Weitz, H. Yi, C.-H. Choi, *Lab Chip* **2018**, *18*, 323.
[25] A. J. Bard, L. R. Faulkner, *Electrochemical Methods: Fundamentals and Applications*, John Wiley & Sons, Inc., New York **2001**.
[26] N. Wu, X. She, D. Yang, X. Wu, F. Su, Y. Chen, *J. Mater. Chem.* **2012**, *22*, 17254.
[27] X. Kang, J. Wang, H. Wu, J. Liu, I. A. Aksay, Y. Lin, *Talanta* **2010**, *81*, 754.
[28] J. Shang, Y. Wan, C. Luo, G. Ye, Q. Geng, A. Auerbach, F. Li, *Proc. Natl. Acad. Sci. USA* **2020**, *117*, 11727.
[29] G. den Hartog, R. M. Schepp, M. Kuijer, C. GeurtsvanKessel, J. van Beek, N. Rots, M. P. Koopmans, F. R. van der Klis, R. S. van Binnendijk, *J. Infect. Dis.* **2020**, *222*, 1452.
[30] A. Baum, B. O. Fulton, E. Wloga, R. Copin, K. E. Pascal, V. Russo, S. Giordano, K. Lanza, N. Negron, M. Ni, Y. Wei, G. S. Atwal, A. J. Murphy, N. Stahl, G. D. Yancopoulos, C. A. Kyratsous, *Science* **2020**, *369*, 1014.
[31] J. S. del Río, O. Y. Henry, P. Jolly, D. E. Ingber, *Nat. Nanotechnol.* **2019**, *14*, 1143.
[32] Q. Li, M. Gordon, C. Cao, K. E. Ugen, D. Morgan, *BMC Neurosci.* **2007**, *8*, 22.
[33] a) D. A. Armbruster, T. Pry, *Clin. Biochem. Rev.* **2008**, *29*, S49; b) Á. Lavín, J. D. Vicente, M. Holgado, M. F. Laguna, R. Casquel, B. Santamaría, M. V. Maigler, A. L. Hernández, Y. Ramírez, *Sensors* **2018**, *18*, 2038.
[34] Y. M. Wang, T. Voisin, J. T. McKeown, J. Ye, N. P. Calta, Z. Li, Z. Zeng, Y. Zhang, W. Chen, T. T. Roehling, *Nat. Mater.* **2018**, *17*, 63.
[35] a) *Handbook of Surface Plasmon Resonance* (Ed: R. B. Schasfoort), Vol. *1*, Royal Society of Chemistry, Cambridge, UK **2017**; b) V. Kandimalla, N. Neeta, N. Karanth, M. Thakur, K. Roshini, B. A. Rani, A. Pasha, N. Karanth, *Biosens. Bioelectron.* **2004**, *20*, 903.
[36] A. Spinelli, G. Pellino, *Br. J. Surg.* **2020**, *107*, 785.
[37] M. A. Ali, X. Wang, Y. Chen, Y. Jiao, N. K. Mahal, S. Moru, M. J. Castellano, J. C. Schnable, P. S. Schnable, L. Dong, *ACS Appl. Mater. Interfaces* **2019**, *11*, 29195.
[38] N. Elgrishi, K. J. Rountree, B. D. McCarthy, E. S. Rountree, T. T. Eisenhart, J. L. Dempsey, *J. Chem. Educ.* **2018**, *95*, 197.